Scholars Journal of Engineering and Technology

OPEN ACCESS

Abbreviated Key Title: Sch J Eng Tech
ISSN 2347-9523 (Print) | ISSN 2321-435X (Online)
Journal homepage: https://saspublishers.com

Computational Fluid Dynamics Analysis and Design of Payload Shroud of Satellite Launch Vehicle

Rakhab C. Mehta[1*]

[1]Department of Aeronautical Engineering, Noorul Islam Centre for Higher Education Kumaracoil, 629180, India

DOI: 10.36347/sjet.2022.v10i04.001 | **Received:** 26.02.2022 | **Accepted:** 01.04.2022 | **Published:** 05.04.2022

***Corresponding author:** Rakhab C. Mehta
Department of Aeronautical Engineering, Noorul Islam Centre for Higher Education Kumaracoil, 629180, India

Abstract | **Original Research Article**

The main focus of the present paper is to computational fluid dynamics analysis and design of payload fairing of satellite launch vehicle at freestream Mach number range of 0.6 - 3.0. Initially, time-dependent compressible three-dimensional Euler equations are solved employing a finite volume discretization method with a multi-stage Runge-Kutta time-stepping scheme to compute surface pressure and aerodynamic coefficients at various payload fairing and at angle of attack up to 5^o with an increment of 1^o. Payload fairing dimensions are selected that satisfies permissible structure load on satellite launch vehicle. Detailed flowfield simulation is carried out on the selected payload fairing employing axisymmetric compressible Reynolds-average Navier-Stokes equations to assess unsteady flowfield characteristics. The numerical simulations are used to locate terminal shock on the payload fairing at transonic Mach number. Unsteady flow characteristics are used to compute acoustic load. Shock standoff distances at supersonic speeds are tabulated and compared with the analytical solution. Schlieren images and oil flow pictures are compared with experimental results and in good agreement. Aerodynamic shape optimization of satellite launch vehicle payload fairing shape has been performed to satisfy structural load at maximum drag and dynamic pressure.

Keywords: CFD; compressible flow; satellite launch vehicle; transonic flow; supersonic flow; shock wave; aerodynamic forces and moments; separated flow.

INTRODUCTION

Payload fairing of a satellite launch vehicle commonly consists of a spherically blunt cone cylinder combination configuration. The payload shroud has to be made larger in diameter as compared to the rest of the vehicle in order to accommodate larger volume of satellite. This leads to a hammer payload fairing configuration. For the combine aerodynamic and structural point of view, the analysis of flow phenomenon on hammer head heat shield is of paramount importance at transonic to supersonic speeds. The structural engineer uses the aerodynamic data to determine skin buckling and bolt placement strength. A high-speed flow past a bulbous payload fairing generates a bow shock wave, which causes a high surface pressure in the spherical-blunt cone section of the payload fairing. The preliminary computational fluid dynamic (CFD) design of payload fairing requires to maintain the vehicle integrity at maximum dynamic load condition during the ascent period of the satellite launch vehicle. It is important here emphasize here that during the ascent phase of the flight of the satellite launch vehicle, the NASA guidelines [1] recommended certain values of cone angle, cone and cylinder lengths, and the boat-tail of payload shroud for restrict the buffeting in the payload fairing at transonic Mach number.

Muraca [2] has developed an empirical method that represents compilation and correlation of wind tunnel experimental data into a set of charts that yield aerodynamic normal load distributions for the various geometrical parameters used in launch vehicle design. Aerodynamic forces and moments can also be calculated using DATCOM for different types of flight vehicle and notably for missiles [3]. The DATCOM is useful for preliminary studies but are not sufficient for detailed flowfield analysis.

An overview of the characterization of the satellite launch vehicle aerodynamic environments has recently been presented by Blevins *et al*., [4] in conjunction with computational fluid dynamics.

Inviscid computational fluid dynamics CFD codes [5] can be used in regions where the contribution of viscous effects is not significant and can be covered with scaling factors such as Reynolds number.

The primary aerodynamic design technique of payload fairing of satellite launch vehicle is based on CFD method and with selected wind-tunnel testing for comparison have been discussed by Pinter *et al*., [6]. Bigarella *et al*., [7] have computed normal force over typical satellite launch vehicles by solving three-dimensional fluid dynamics equations. The use of CFD provides a unique capability in design and analysis of payload fairing for satellite launch vehicle. The database of launch vehicles [8, 9] are useful to diagnosis the aerodynamics design parameters of complex launch vehicle. Time-accurate CFD simulation of transonic flow over a boubous Configuration has been presented by Ozair *et al*., [10]. Unsteady numerical analysis of transonic buffet flow around a hammerhead payload fairing has been carried by Liu *et al*., [11]. Yanamashetti *et al*., [12] have simulated flow over blunt-nosed heat shield at transonic Mach numbers. Sunil *et al*., [13] have done aerodynamic shape optimization of payload fairing boat-tail for various diameter ratios. CFD analysis of imaging quality of laser communication system on missile in the aerodynamic environment is investigated by Jiang *et al*., [14]. Computational and experimental unsteady pressures and loads for different nose shapes for the space launch system has been investigated by Alter *et al.,* [15] and Brauckmann *et al*., [16]. Unsteady flowfield characteristics over blunt bodies at high speed are numerical simulated by Mehta [17]. Analysis of Ares Crew launch vehicle transonic flow and buffet testing analysis are presented in Refs [18, 19]. Dotson *et al*., [20] observed that a vortex-Induced flow at transonic speed may detrimental to launch vehicle. Contours of density of Navier-Stokes flow solver can be employed by digital holographic interferometry to detect the vehicle surface-to-air missile [21].

In additions to integrated aerodynamic force and moment testing, CFD solutions are generated for many vehicles of the same conditions that are tested in the wind tunnel. These major inputs to structural loads analysis are developed by integrating the numerical solutions data circumferentially along the length of the payload fairing centerline axis. This distributed aerodynamic load is a paramount component quantity used to design the primary structure of the heat shield configuration. A CFD technique can provide rapid computation of aerodynamic distributed loads on the heat shield as compared the data from wind tunnel testing.

A schematic sketch of the complex flowfield over the payload shroud is shown in Fig 1(a) at transonic speeds. The diagram depicts the expansion fan on cone-cylinder junction, sonic line, supersonic pocket, terminated shock and shock wave turbulent boundary layer interaction over the cylinder region at the transonic speeds. Separated flow in the boat tail region is occurred attributed to change in geometry. A shear layer is formed combined with a recirculation flow.

Figure 1(b) depicts complex supersonic flowfield over a payload shroud. The flowfield is completely altered as compared to the transonic flowfield. The flow downstream of the boat-tail through an expansion fan with a resulting shear layer. The pressure in the recirculation region is generally uniform and below that of the freestream pressure. As the shear layer impinges on the downstream wall, the flow turns back toward the freestream direction and a recompression shock wave typically appeared. For the sake of completeness, Figure 1(c) describes the wave propagation in compressible flow to illustrate wave characteristics in different speed regime.

The paper presents a CFD in house developed flow solver to obtain the geometrical parameters of the payload shroud to maintain the structural integrity of the launch vehicle. Initially, a numerical simulation of time-dependent, three-dimensional, compressible Euler equations is carried out employing three-stage Runge-Kutta time-stepping scheme. The numerical scheme is second-order accurate in space and time. A local time stepping is used to achieve steady-state solution. The purpose of the present study is to obtain the aerodynamic forces at a freestream Mach number of 1.2 and 1.8 and an angle of attack up to 5^{o} with an increment of 1^{o}. The numerical method includes the different geometrical parameters of the bulbous heat shield on normal force distribution along the heat shield to satisfy structural design criteria. The computations of aerodynamic forces will be helpful for adequate for preliminary design of the bulbous pay load shroud for the structural integrity of the payload shroud. On the selected payload shroud which satisfy the structure load criteria, axisymmetric compressible Reynolds averaged Navier-Stokes (RANS) equations are solved to get steady and unsteady flow characteristics in order to assess the acoustic load. A global time stepping used here to get time accurate solution. The aerodynamic forces and moments are evaluated at different freestream Mach numbers and geomatical parameters of the payload fairing of satellite launch vehicle during ascent phase.

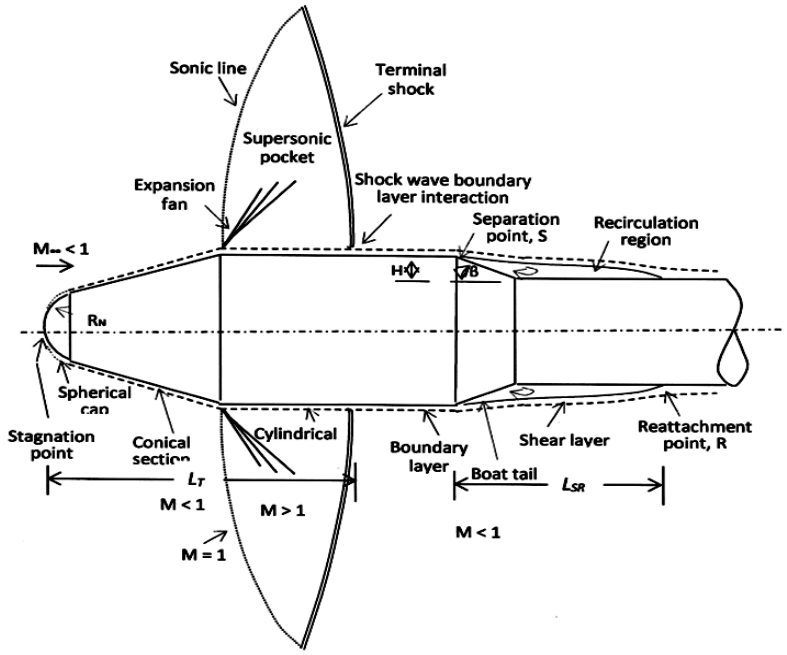

Fig 1(a): Schematic sketch of flow field over payload shroud at transonic speed

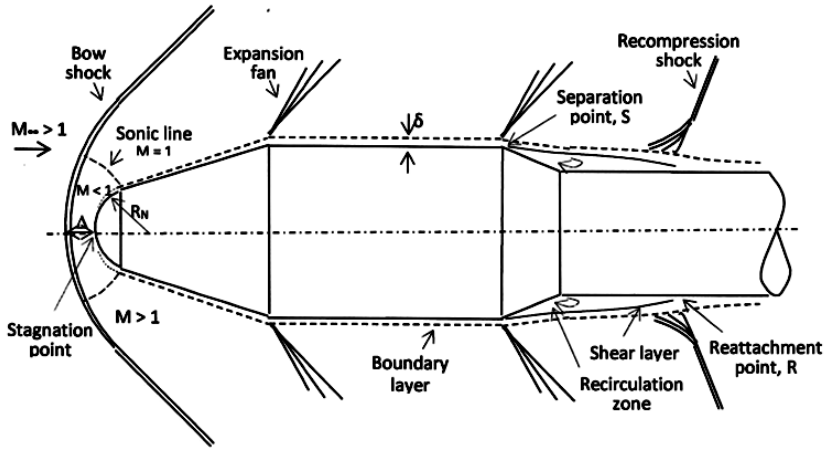

Fig 1(b): Schematic sketch of flow field over payload shroud at supersonic speed

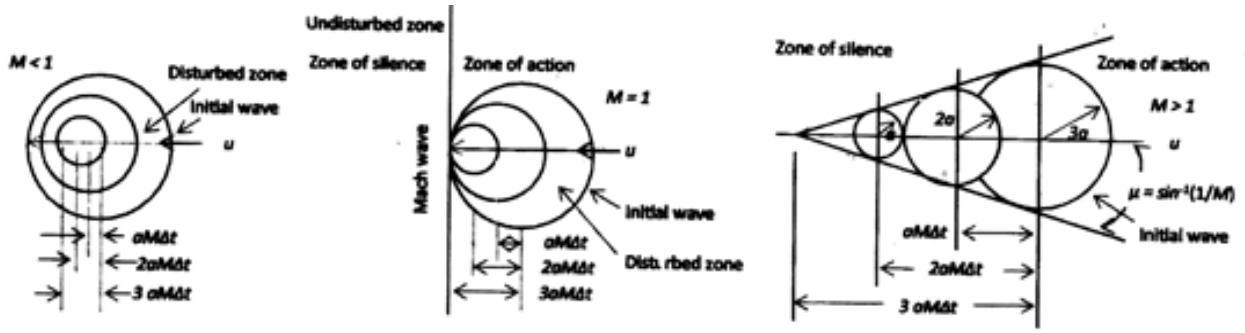

Fig 1(c): Schematic sketch of wave propagation in compressible flow

2. NUMERICAL ANALYSIS

Governing Equations

The fluid motion of governed by time dependent three-dimensional compressible inviscid equations which express the conservation of mass, momentum and energy in the absence of external forces. The high-speed flow over the payload fairing is expressed by Euler equations of motion in a flux vector form as:

$$\frac{\partial \mathbf{U}}{\partial t}+\frac{\partial \mathbf{F}}{\partial x}+\frac{\partial \mathbf{G}}{\partial y}+\frac{\partial \mathbf{H}}{\partial z}=0 \quad \text{..... (1)}$$

Where

$$\mathbf{U}=\begin{bmatrix}\rho\\ \rho u\\ \rho v\\ \rho w\\ \rho e\end{bmatrix},\ \mathbf{F}=\begin{bmatrix}\rho u\\ \rho u^2+p\\ \rho uv\\ \rho uw\\ (\rho e+p)u\end{bmatrix},\ \mathbf{G}=\begin{bmatrix}\rho v\\ \rho uv\\ \rho v^2+p\\ \rho vw\\ (\rho e+p)v\end{bmatrix},\ \mathbf{H}=\begin{bmatrix}\rho w\\ \rho uw\\ \rho vw\\ \rho w^2+p\\ (\rho e+p)w\end{bmatrix}$$

are the ***U*** state vector conserved quantities with ρ, u, v, w and e denoting the density, Cartesian velocity components, and the specific total energy, respectively, and inviscid flux vectors, ***F***, ***G*** and ***H*** in the Cartesian coordinates x, y and z. With the ideal gas assumption, the pressure and total enthalpy can be expressed as:

$$\rho\, e=\frac{p}{(\gamma-1)}+\frac{1}{2}\rho\left(u^2+v^2+w^2\right) \text{..... (2)}$$

here γ is the ratio of specific heats.

Numerical algorithm

To simplify the spatial discretization in numerical technique, Eq. (1) can be written in the integral form over a finite computational domain Ω with the boundary Γ as:

$$\int_{\Omega}\mathbf{U}d\Omega+\int_{\Gamma}(\mathbf{E}+\mathbf{F}+\mathbf{G})d\Gamma=\int_{\Omega}\mathbf{H}d\Omega \quad \text{..... (3)}$$

Here Ω is a control volume with surface Γ. The contour integration around the boundary of the cell is performed in anticlockwise sense in order to keep flux vectors normal to boundary of the cell. The computational domain has a finite number of non-overlapping hexahedral cells. In a cell centred finite volume method, the flux variables are stored at the centroid of the grid cell and the control volume is formed by the cell itself. The conservation variables within the computational cell are represented by their average values at the cell centre.

The inviscid fluxes are computed at the cell-centre resulting in flux balance. The summation is carried out over the eight edges of the cell. The space discretization scheme shares the reconstruction of the conservative variables of cell interfaces but differ in the evaluation of fluxes in time stepping. The inviscid fluxes are obtained from Roe's approximate Reimann solver. The numerical scheme is advanced in time with a third order Runge-Kutta method [22]. AUSM+ scheme is employed here to evaluate the inviscid fluxes by splitting them as a convective and pressure terms. The spatial discretization described above reduces the integral equation to semi-discrete ordinary differential equations. The numerical algorithm is second-order accurate in space discretization and time integration. The numerical scheme is stable for a Courant number ≤ 2. Local time steps are used to accelerate to a steady-state solution by setting the time-step at each point to the maximum value allowed by the local Courant-Friedrichs-Lewy (CFL) condition.

Initial and boundary conditions

To solve the equations of motion, one has to have the initial boundary conditions, which defines a particular problem. At the inflow, all the flow variables are taken at the freestream values as tabulated in Table 1.

At a solid wall, the velocity tangential to the boundary is applied since the flow is inviscid. At transonic freestream Mach number, the computational domain of dependence is unbounded, and the implementation of boundary and initial conditions become critical, the known physically acceptance of far-field boundary conditions usually limit the flow variables to asymptotic values at large distance from the payload fairing. Therefore, suitable coordinate stretching and placement of the far-field boundary condition have been considered in numerical simulations. The freestream conditions are prescribed on the outer boundary. For supersonic flow, all of the flow variables are extrapolated from the vector of conserved variables ***U***. An image cell is imposed to the solved variables at the line of symmetry ahead of the vehicle.

Table 1: Initial conditions

M_∞	$p_\infty \times 10^5$ Pa	T_∞ K
0.8	0.83	266
0.9	0.787	258
0.95	0.766	254
1.0	0.93	250
1.1	0.68	241
1.2	0.64	232
1.5	0.45	207
1.75	0.36	186
2.0	0.285	166
2.5	0.184	134
3.0	0.122	107

Table 2: NASA criteria for buffet free payload shroud

Model	α_1, deg	l_1/D	l_2/D	d/D	α_2, deg
NASA [1]	≤ 15	≥ 0.80	> 1.50	0.9 - 1.11	Not critical

Table 3: Dimensions of various payload fairing

Payload shroud	R_N, m	α_1, deg	D, m	$(l_1 + l_2)$ m	α_2, deg
SLV-1	1.07	15^o	3.6	9.75	38^o
SLV-2	0.75	15^o	3.4	9.25	36^o
SLV-3	0.75	15^o	3.4	9.75	18^o
SLV-4	0.70	20^o	3.4	8.82	37^o
SLV-5	0.75	15^o	3.4	8.71	30^o
SLV-6	1.00	15^o	3.4	8.00	30^o
SLV-7	0.70	20^o	3.2	8.32	15^o

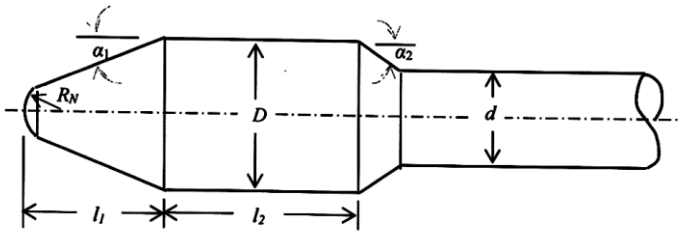

Fig 2: Geometrical detail of payload shroud

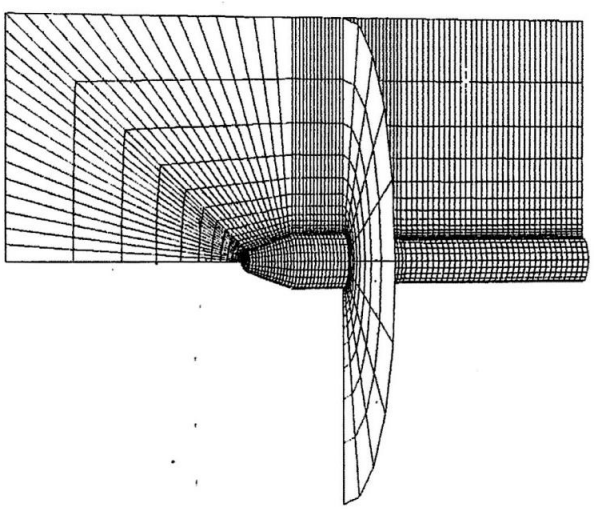

Fig 3: Computational grid over payload shroud

2.5 Dimension of Payload Shroud and Computational Grid

Table 2 and Fig 2 shows the NASA recommended geometrical dimensions for payload shroud. The geometrical parameters α_1, α_2, l_1, l_1, R_N, D and d are employed to compute the aerodynamic loads. The dimensions of the payload shroud are in the range of the NASA recommended criteria. We have carried out numerical simulations of several configurations and the dimensions are tabulated in Table 3.

The body-oriented grids are generated using a homotopy one-to-one and onto technique in conjunction with finite element method [23]. The stretched grids are generated in an orderly manner. Efficient computation of cell volume in flow prediction is used as described in Ref. [24]. A non-uniform and non-overlapping structured computational cell is generated for numerical simulations. The grid-stretching factor is selected as 4, and the outer boundary of the computational domain is maintained as 3.5 − 4.5 times maximum diameter D of the payload fairing. In the downstream direction, the computational boundary is about 6 - 9 times the diameter of the module; D. The computational domain depends on freestream Mach number. Figures 3 show three-dimensional view of grid over the payload fairing. The grid arrangement is found to yield a relative difference of about ± 3% in the pressure peak, which is in the same range as the stagnation pressure measurement error in the wind-tunnel. The convergence criterion is based on the difference in density values at any of the grid points, between two successive iterations $\left|\rho^{n+1} - \rho^{n}\right| \leq 10^{-5}$ where n is time-step counter. The numerical computations were carried out with various grid arrangements in order to meet a grid independency check. Grids typically contained 46 cells in the longitudinal direction, 45 cells in the transverse direction, and 15 – 25 cells in the body-normal direction. The minimum grid size in the normal direction of the payload fairing is about 1.70×10^{-4} m. The internal grid cells were constructed so that all of the nose pressure ports coincide with the center of a finite volume cell face.

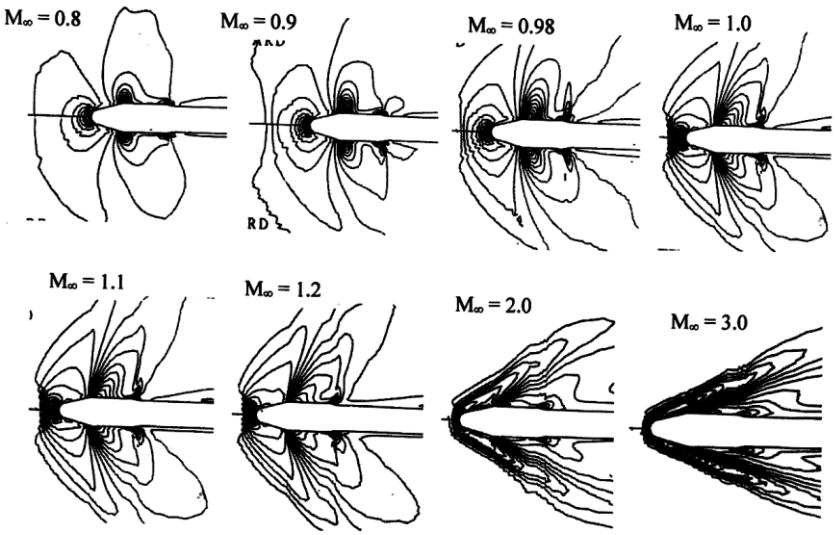

Fig 4: Density contour over payload shroud at angle of attack $\alpha = 1^o$

Three-dimensional flow characteristics

For the sake of brevity, we are presenting windward and leeward sides density contours over heat shield at $M_\infty = 0.8$ to 3.0 at $\alpha = 1^o$ degree is depicted in Fig 4 for payload fairing of SLV-3 of Table 3.

It can be seen from the density contours that the flowfield characteristics depend on flight Mach numbers. The density contours in Fig. 4 (in the first row) exhibit the transonic flow behaviour of flowfield over the payload fairing. The terminal shock moves downstream on the payload fairing for $M_\infty < 1$. It can be observed the formation of terminal shock and supersonic pocket at transonic speeds. The movement of terminal shock shows function of freestream transonic Mach number.

Fig. 4 (in the second row) shows formation of bow shock over forebody and presence of weak oblique shocks downstream of the cone-cylinder junction of the payload fairing for $M_\infty > 1$. The expansion and compression on the shoulder points of the payload fairing are visible in the density contours. A formation of the bow shock wave stands in front of the blunt body and forms an embedded subsonic flow region around the blunt-spherical cone region of the payload shroud. It also lies between the bow shock wave and body surface and bounded by sonic lines extending from the body of the heat shield to the bow shock wave. An expansion fan over the shroud of the heat shield can also be observed in the Mach contour plots.

The pressure coefficient $Cp = [(p_o - p_\infty)/q_\infty]$ in windward and leeward sides is shown in Fig. 5(a) and (b) respectively, where p_∞ is freestream pressure and q_∞ is freestream dynamic pressure. Stagnation point pressure coefficient is compared with wind tunnel results. The comparison shows good agreement between them. It can be seen from Fig. 5 that the stagnation point pressure coefficient increases with increase of M_∞. As the Mach number increases the bow shock wave comes close to the heat shield. Pressure versions along the payload also reveals the flow characteristic of transonic and supersonic speeds.

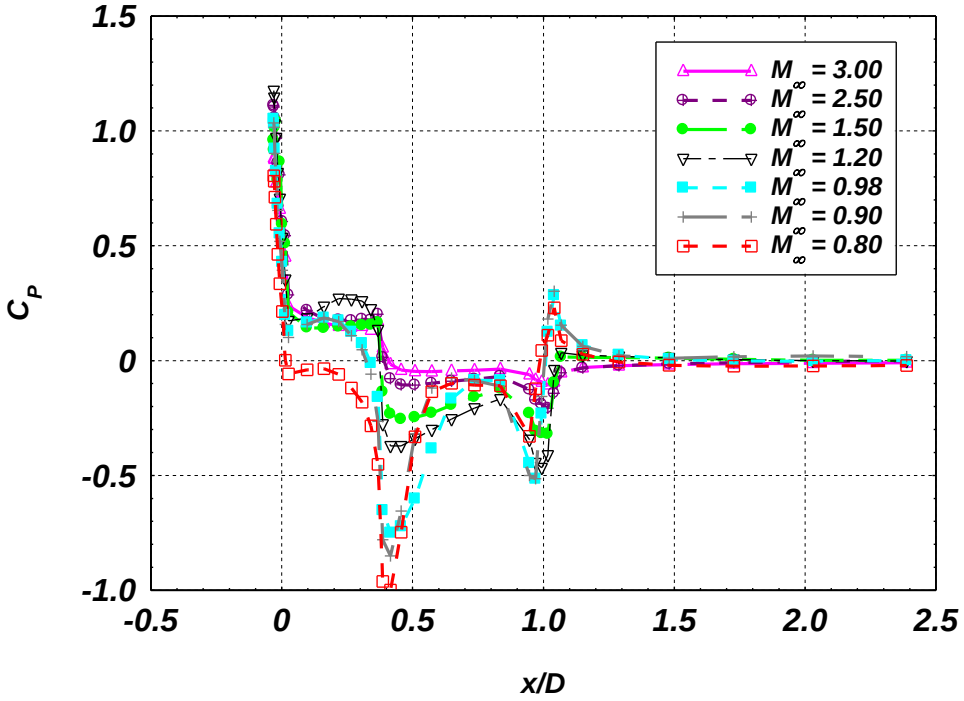

Fig 5 (a): Variation of windward pressure coefficient at angle of attack $\alpha = 1^o$

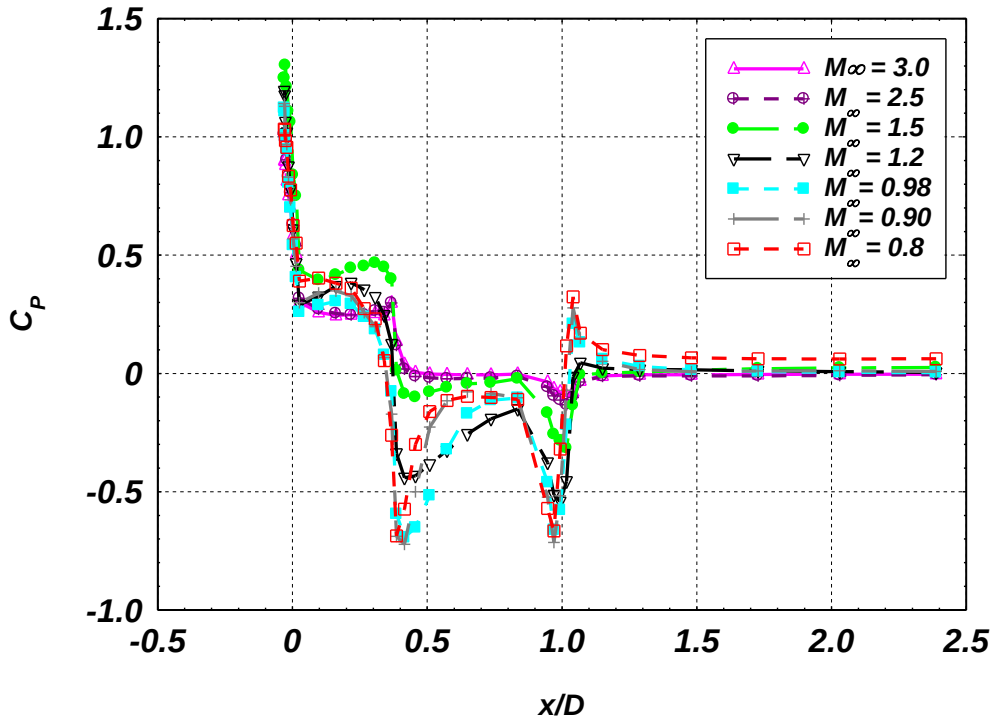

Fig 5(b): Variation of leeward pressure coefficient at angle of attack $\alpha = 1^o$

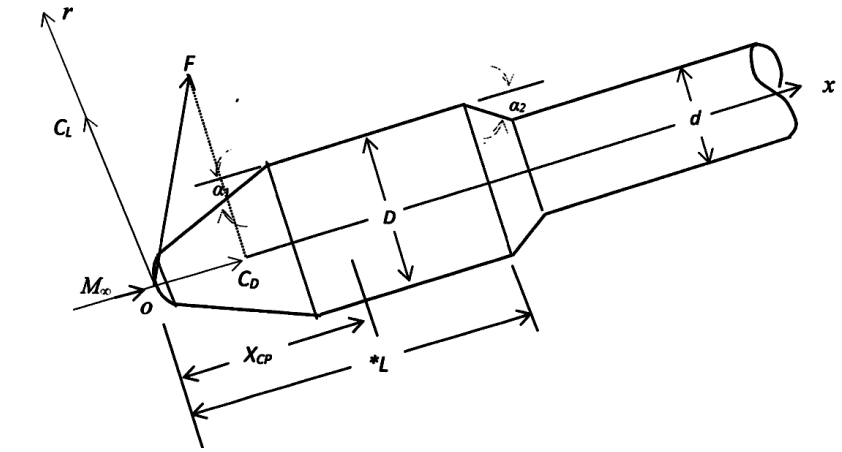

Fig 6: Aerodynamic forces and moment in pitch plane at an angle of attack

Aerodynamic load computations

The normal load distribution C_N can be computed employing following expression

$$S\frac{dC_N}{dx} = 2\pi r\int_0^L \int_0^\pi \{Cp(\phi,x)\cos\phi d\phi\}dx \quad \ldots\ldots\ldots\ldots (5)$$

Where S is reference area at the booster diameter of the payload shroud d. ϕ is circumferential direction. The normal load distribution is computed along the payload shroud at freestream Mach number range 0.6 to 3.0 for the payload fairing SLV-7 of Table 3. Figure 6 illustrates aerodynamic forces and moment in the pitch plane at an angle of attack.

The structure integrity of the payload fairing requires a detailed description of normal force and location of centre of pressure X_{CP}. The distributed aerodynamic coefficient is defined as product of the normal force coefficient derivative with respect to the heat shield length and with reference area term. By integrating the running aerodynamic load over the length of the payload fairing and dividing by a reference area, a total normal force coefficient slope can be obtained. Using the computed pressure distribution, the normal force coefficient is evaluated using the following equation

$$Cn_\alpha = \frac{4}{S}\int_0^\pi Cp(\phi,x)rd\phi \quad \ldots\ldots\ldots\ldots\ldots (6)$$

The centre of aerodynamic pressure is evaluated using the following expression

$$X_{CP} = \frac{\int_0^L \int_0^\pi [Cp(\phi,x)r\cos\phi d\phi]xdx}{\int_0^L \int_0^\pi [Cp(\phi,x)r\cos\phi d\phi]dx} \quad \ldots\ldots\ldots\ldots (7)$$

The value of X_{CP} is calculated from the stagnation point of the heat shield. The values of normal force coefficient and centre of pressure are shown in for the payload fairing in Table 4. Figure 7(a) and (b) presents variation of normal force and center of pressure at various freestream Mach number for SLV-7.

Table 5 depicts comparison between the numerical results with the wind tunnel data of payload shroud SLV-7 of Table 3. The computed values show about ± 10% error with the experimental data. This error band is within the uncertainty limit of the experimental data. This discrepancy in the variation of aerodynamic load with the experimental data is attributed that did not reflect significant flow separation. The accuracy of the numerical results has been shown by comparison with wind tunnel pressure and force data. The aerodynamic drag coefficient C_D computed using following relation.

$$C_D = \frac{2\pi r\int_0^\pi Cp\sin(\phi,x)d\phi}{\frac{1}{2}\rho_\infty V_\infty^2 S_0} \quad \ldots\ldots\ldots\ldots (8)$$

Aerodynamic drag for payload shroud of SLV-7 is shown in Table 6. Aerodynamic drag is function of freestream Mach number and maximum drag is found at about M_∞ = 1.2.

In the next section we will compute viscous flow over SLV-1, SLV-5 and SLV-7. The viscous solution will compute the effect of shock wave boundary layer interaction over the payload and geometrical induced flow separation in the boat tail region. This analysis will also compute unsteady flow caused by shock wave boundary layer interaction.

Table 4: Aerodynamic forces and moment for various payload shroud of satellite launch vehicle

M_∞	SLV-1		SLV-2		SLV-3		SLV-4		SLV-5		SLV-6		SLV-7	
	$C_{N,\alpha}$	X_{CP}	$C_{N,\alpha}$	X_{CP}	$C_{N,\alpha}$	X_{CP}	$C_{N,\alpha}$	X_{CP}	$C_{N,\alpha}$	X_{CP}	$C_{N,\alpha}$	X_{CP}	$C_{N,\alpha}$	X_{CP}
0.75	1.67	5.40	0.94	1.25	1.12	1.31	0.94	1.23	0.94	1.25	1.12	3.31	1.12	1.31
0.80	2.03	5.03	1.28	1.75	1.13	1.56	1.28	1.75	1.28	1.75	1.13	1.58	1.13	1.58
0.90	-	-	2.34	2.35	2.36	2.35	2.34	2.35	2.34	2.35	2.36	2.35	2.36	2.35
0.95	4.62	4.82	2.50	1.86	2.54	2.13	2.50	1.86	2.50	1.86	2.84	2.13	2.54	2.13
0.98	-	-	3.03	2.04	2.74	2.07	3.03	2.04	3.03	2.04	2.74	2.07	2.74	2.06
1.00	4.70	4.21	3.27	2.05	3.10	3.73	3.27	2.05	3.27	2.05	3.10	2.33	3.10	2.38
1.20	4.85	3.23	3.78	2.96	2.80	2.13	3.78	2.96	3.87	2.96	3.23	2.85	3.73	2.85
1.40	4.10	2.84	2.90	2.96	3.22	2.49	2.90	2.29	2.90	2.29	2.80	2.13	2.80	2.13
1.60	3.74	2.60	3.38	3.38	2.90	2.27	3.38	2.70	2.38	2.70	3.23	1.49	2.32	2.49
1.80	3.48	2.43	3.87	2.48	2.69	2.12	3.07	2.28	3.07	2.48	2.90	2.27	2.90	2.27
2.00	3.48	2.43	2.81	2.27	2.83	2.32	2.81	2.27	2.82	2.27	2.69	2.12	2.69	2.12
3.00	3.30	2.36	2.81	2.29	3.12	3.29	2.72	2.29	2.72	2.29	2.83	2.35	2.83	2.34

Table 5: Aerodynamic forces and moment for SLV-7

M_∞	C_N/rad	X_{cp}, m	C_N/rad	X_{cp}, m
	Numerical		Experimental	
1.2	4.28	2.69	3.97	2.79
1.6	3.92	2.97	3.57	2.52
1.8	3.91	2.94	3.27	2.34

Table 6: Aerodynamic drag for payload shroud of SLV-7

M_∞	0.80	0.90	0.98	1.00	1.20	1.60	1.80	2.0	3.0
C_D	0.41	0.51	0.58	0.88	0.98	0.94	0.86	0.8	0.7

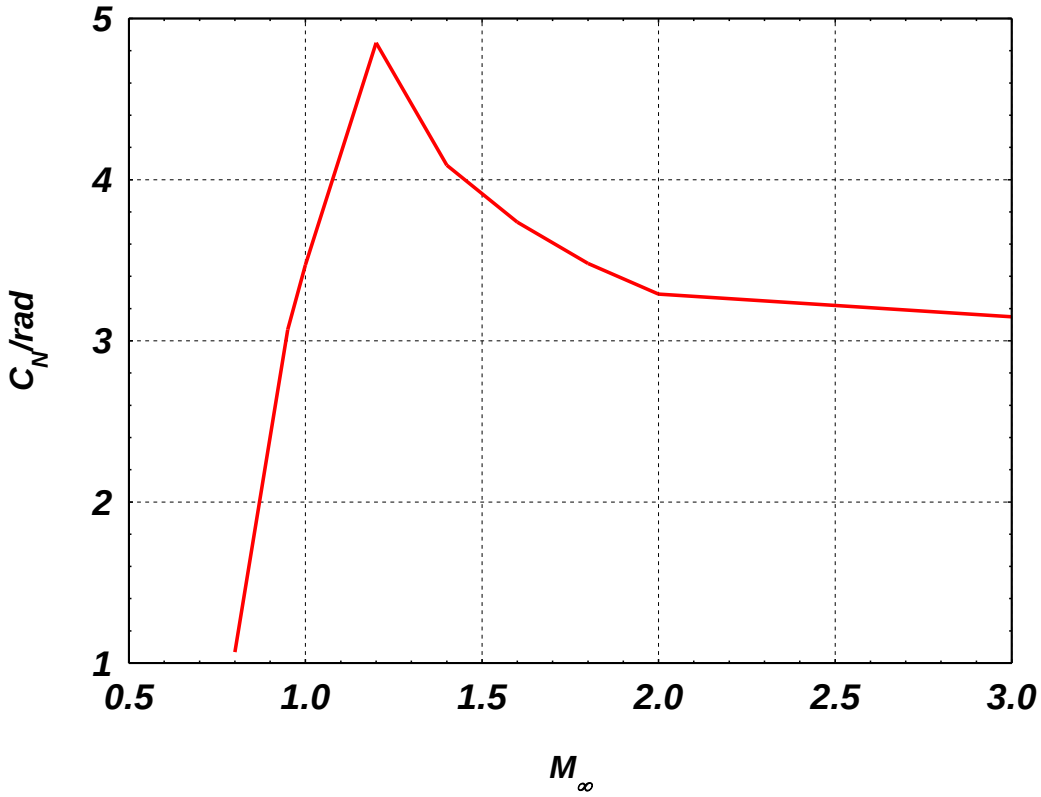

Fig 7(a): Variation of normal force vs. Mach number for SLV-7

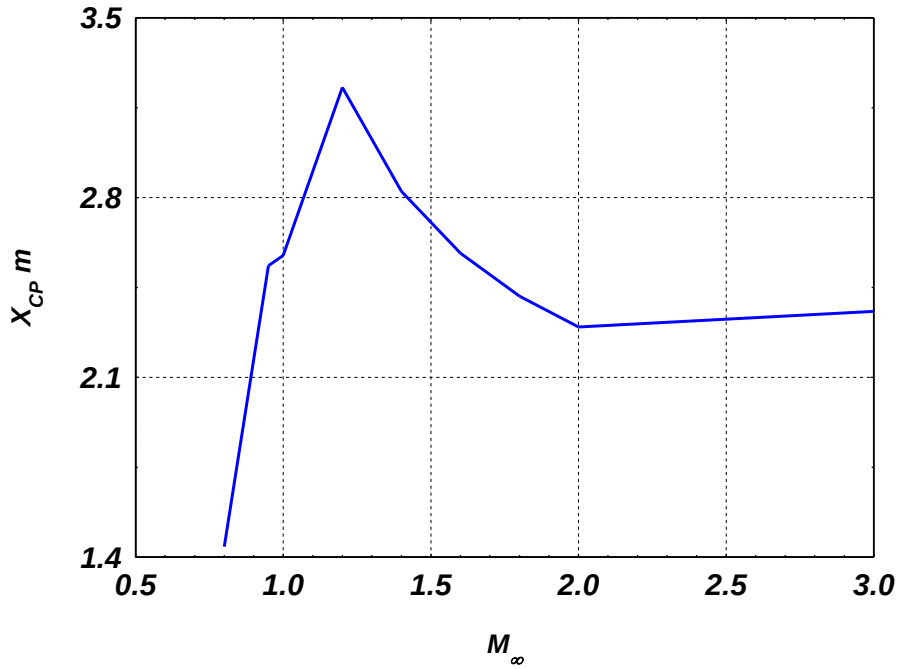

Fig 7(b): Variation of aerodynamic centre of pressure vs. Mach number for SLV-7

Numerical solution of axisymmetric Reynolds-averaged Navier-Stokes equations

A numerical simulation of the time-dependent, compressible, turbulent, axisymmetric Reynolds-averaged Navier-Stokes equations (RANS) are written as in the conservation form of mass, momentum and energy. The closure of the system of equation is achieved by introducing the Baldwin-Lomax [25] turbulence model. The algebraic model utilizes the vorticity distribution to determine the scale length, has been extensively used solving the RANS.

To simplify the spatial discretization in numerical technique, RANS equations can be written in the integral form over a finite computational domain. The contour integration around the boundary of the cell is performed in anticlockwise sense in order to keep flux vectors normal to boundary of the cell. The computational domain Ω is having a finite number of non-overlapping quadrilateral cells. The conservation variables within the computational cell are represented by their average values at the cell centre. The inviscid fluxes are computed at the cell-centre resulting in flux balance. The summation is carried out over the four edges of the cell. The derivatives of primitive variables in the viscous flux are evaluated by using the method of lines. The cell-centred spatial discretization scheme is non-dissipative, therefore, artificial dissipation terms are included as a blend of a Laplacian and bi-harmonic operator in a manner analogous to the 2^{nd} and 4^{th} differences. The blend of second and fourth differences provides third order back ground dissipation in smooth region of the flow and first-order dissipation in shock waves.

The spatial discretization described above reduces the integral equation to semi-discrete ordinary differential equations (ODE). The ODE is solved using multi-stage Runge-Kutta time stepping scheme [22]. The numerical algorithm is second-order accurate in space discretization and time integration. The scheme is stable for a Courant number ≤ 2. Global time steps are used to get time accurate.

Initial and boundary conditions for viscous flow

At transonic freestream Mach number, the computational domain of dependence is unbounded, and the implementation of boundary and initial condition become critical, the known physically acceptance far-field boundary conditions usually limit the flow variables to asymptotic values at large distance from the heat shield. On the other hand, adjustment of the grid points spacing to the body demands fine dimensions to yield reasonable resolution of the boundary layer. Therefore, suitable coordinate stretching and placement of the far-field boundary condition must be performed in numerical simulations. The freestream conditions are prescribed on the outer boundary. On the heat shield wall, no-slip and adiabatic conditions are imposed. At the line of symmetry ahead of the heat shield an image cell is imposed on the solved variables. At the inflow, all the flow variables are taken at the freestream values as tabulated in Table 1.

For the subsonic flow ($M_\infty \leq 1$), non-reflecting far-field boundary conditions are applied at the outer boundary of the computational domain. For supersonic flow ($M_\infty > 1$), all of the flow variables are extrapolated at the outer from the vector of conserved variables $\boldsymbol{U}$.

At the line of symmetry ahead of the heat shield, an image cell is imposed to the solved variables.

Model and Computational Grid

The body-oriented grids are generated using a homotopy scheme in conjunction with finite element method [23]. The stretched grids are generated in an orderly manner. A non-uniform and non-overlapping structured grid is generated for numerical simulations. The grid-stretching factor is selected as 5, and the outer boundary of the computational domain is maintained as 3.5 − 4.5 times maximum diameter *D* of the heat shield. In the downstream direction, the computational boundary is about 6 − 9 times the diameter of the module; *D*. Figure 8 shows view of grid over the payload shroud of SLV-7. We have displayed grid with one-plane rotation in order to check the axisymmetry of grid distribution over the heat shield. The grid arrangement is found to yield a relative difference of about ± 3% in the pressure peak, which is in the same range as the pressure measurement error in the wind tunnel with a blockage ratio of about 0.3%. The convergence criterion is based on the difference in density values at any of the grid points, between two successive iterations $\left|\rho^{n+1}-\rho^{n}\right| \leq 10^{-5}$ where *n* is time-step counter. The numerical computations were carried out with different grid arrangements in order to get a grid independency check. The computation is performed using 132 × 62 grid points over the hemisphere-cylinder. The finer grid near the wall helps to resolve the boundary layer. The coarse grid economizes the computer time. The minimum grid size in the normal direction of the heat shield is about 1.70×10^{-4} m. A global time-step Δt is used rather than the grid varying time-step to simulate time accurate solution.

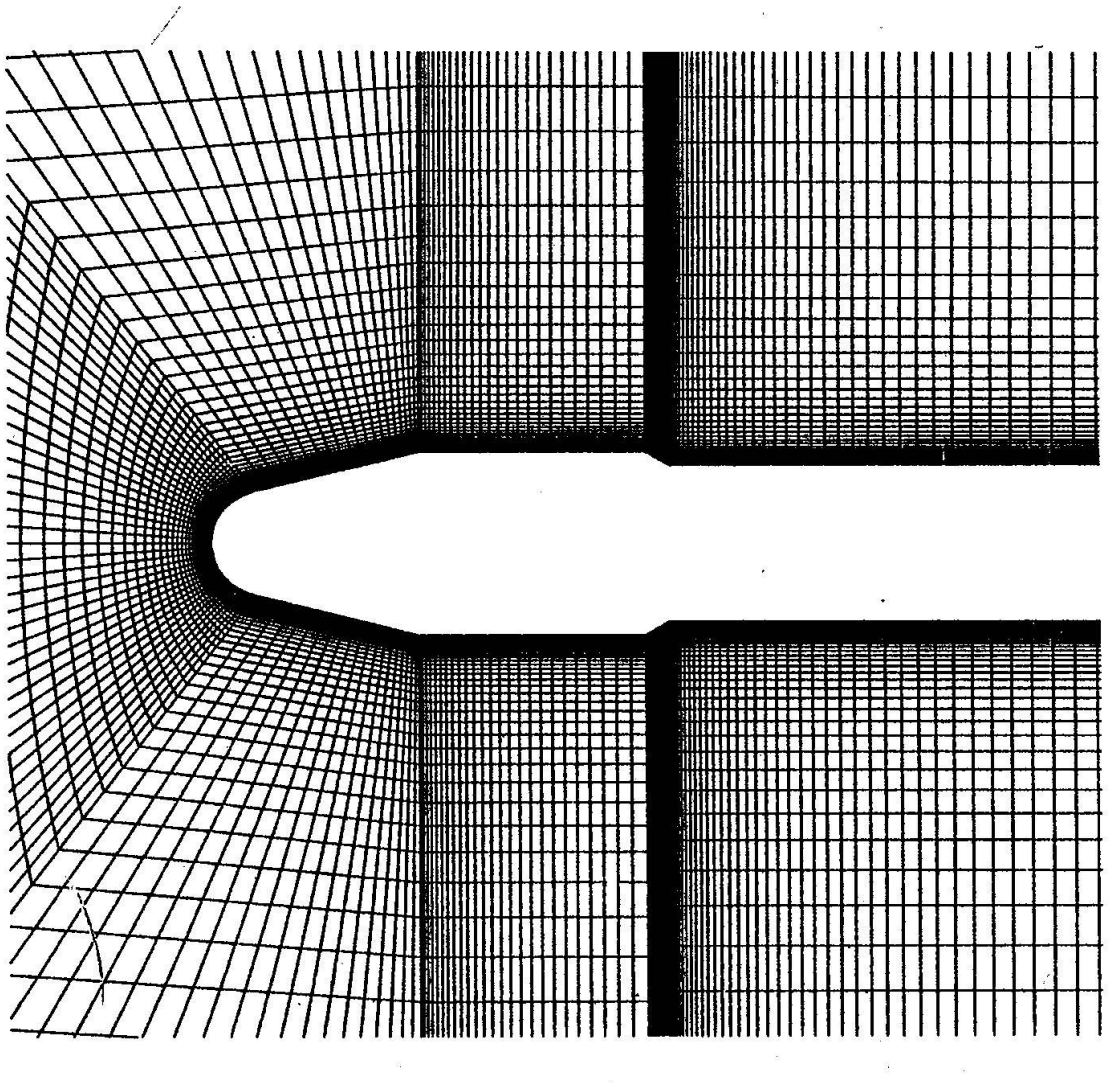

Fig 8: Axisymmetric computational grid over payload shroud of SLV-7

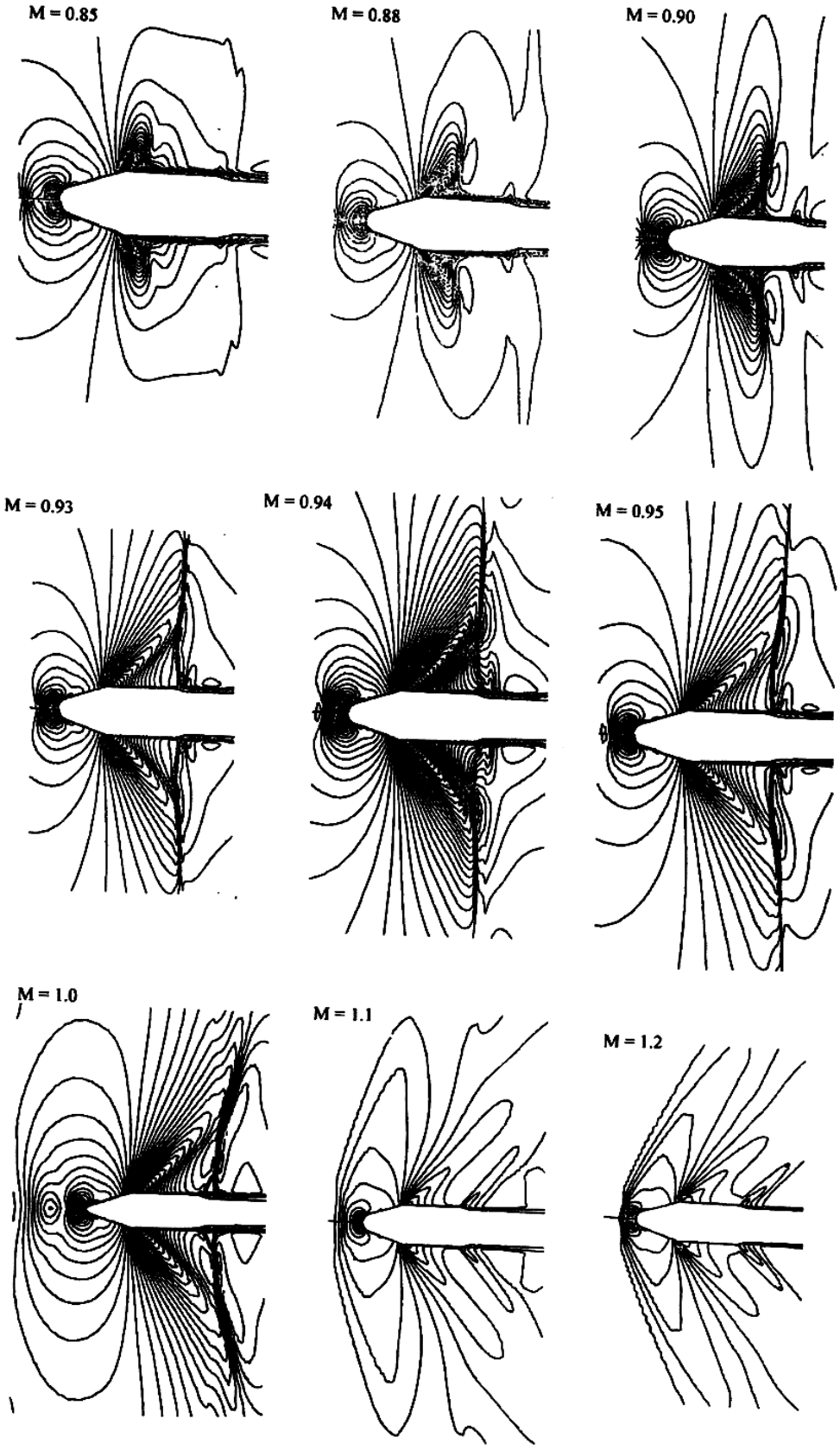

Fig 9: Density contours over payload shroud of SLV-5

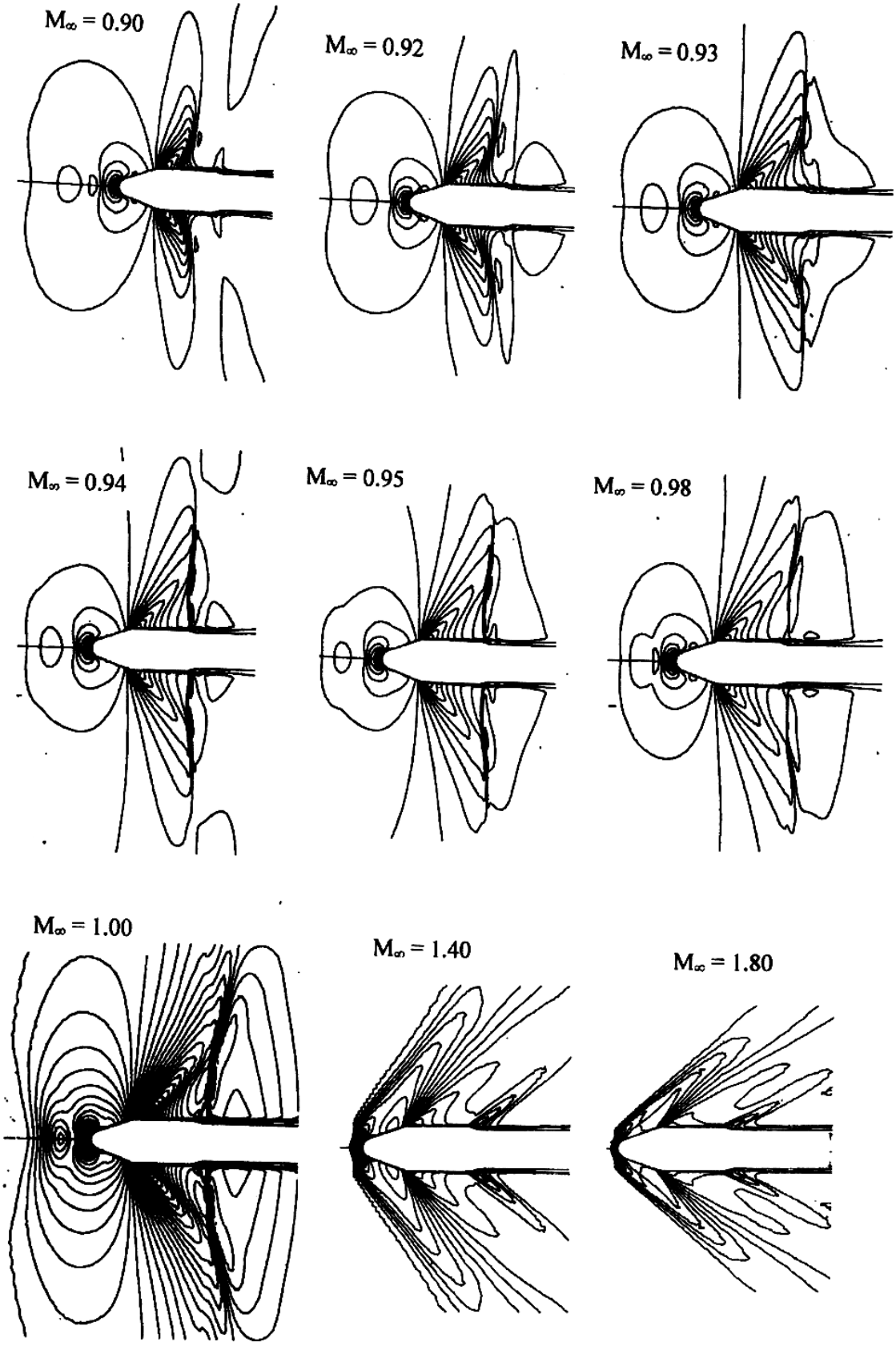

Fig 10: Density contours over payload shroud of SLV-6

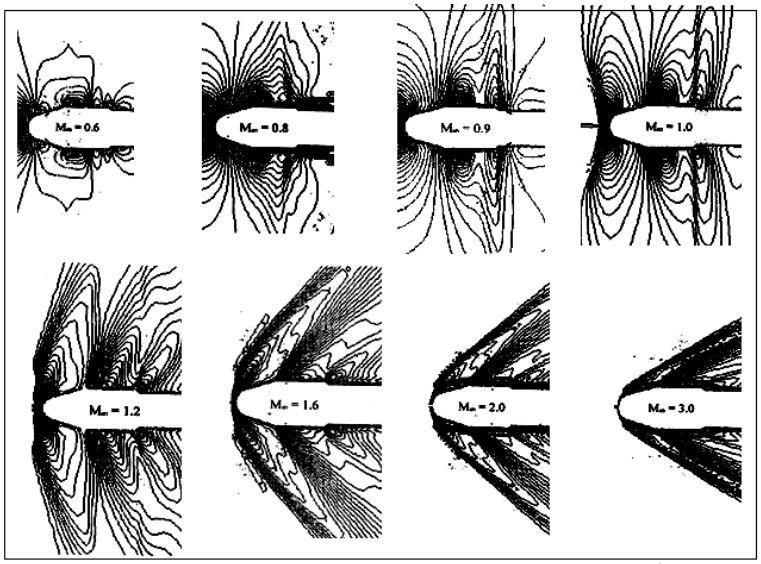

Fig 11: Density contours over payload shroud of SLV-7

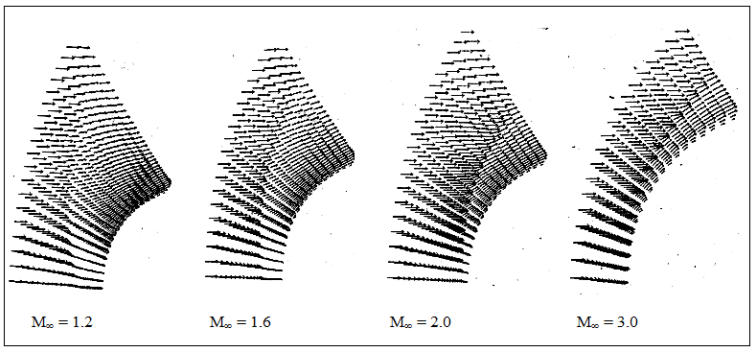

Fig 12: Vector field over payload shroud of SLV-7

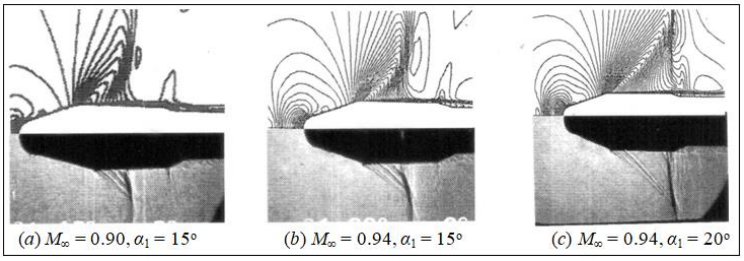

Fig 13: Comparison between density contour and schlieren picture SLV-7

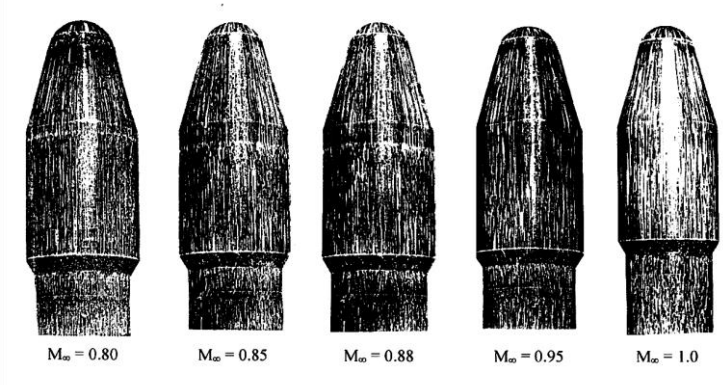

Fig 14: Oil flow simulation over payload shroud of SLV-7

Table 7: Location of terminal shock on payload shroud SLV-7

M_∞	L_T/D, measured	L_T/D, computed
0.80	1.19	1.186
0.90	1.54	1.538
0.95	2.17	2.15
1.00	2.59	2.581

Table 8: Separation length (L_H) in boat tail region for various scale model of payload shroud of SLV-7

M_∞	Model 1:52	Model 1:26	Model 1:14	Flight
0.80	6.87	6.90	7.10	7.0
0.85	7.11	—	—	—
0.88	7.30	7.30	7.83	7.50
0.90	7.66	7.70	8.55	8.00
0.95	8.30	9.50	11.22	10.42
0.98	10.22	10.68	11.88	10.94
1.00	11.10	12.00	13.12	12.77
1.10	7.00	7.22	7.70	7.45
1.20	6.54	6.88	7.44	7.30
1.30	6.33	6.47	7.00	6.88
1.40	6.00	6.33	6.70	6.48
1.50	5.90	—	6.50	—
1.60	5.66	5.80	6.25	6.12
2.00	5.11	5.25	5.45	5.40
Re_D	1.5×10^6	3.0×10^6	4.0×10^6	40.0×10^6

Table 9: Bow shock wave standoff distance for payload shroud of SLV-7

M_∞	Δ/R_N, computed	Δ/R_N, Zierep *et al.*,
1.2	1.15	0.122
1.4	0.55	0.559
1.6	0.30	0.348
1.8	0.26	0.236
2.0	0.24	0.171
2.5	0.18	0.097
3.0	0.10	0.045

RESULTS AND DISCUSSION

Flowfield characteristics over axisymmetric payload fairing

Figures 9–11 show density contours over payload shroud of SLV-5, SLV-6 and SLV-7. The density contours have captured all the essential flow field characteristic of transonic and supersonic Mach numbers. The density contours are function of payload dimensions as well as freestream Mach number. Nomenclature of the terminal shock distance, length of separated flow in the boat tail and bow shock standoff distance is shown in Fig. 1(*a*) and (*b*). Table 7 shows the location of terminal shock on payload shroud SLV-7. It can be observed the shock movement is non-linear function of freestream Mach number. It increases with increasing freestream Mach number. Table 8 shows separation length (L_H) in boat tail region for various scale model of payload shroud of SLV-7. Figure 12 shows the vector field over payload shroud of SLV-7 and Table 9 shows the standoff distance of the bow shock from the blunt-nose. Figure 13(*a*), (*b*) and (*c*) shows comparison between density contour and schlieren picture SLV-7 for $M_\infty = 0.90$, $\alpha_1 = 15^o$, $M_\infty = 0.94$, $\alpha_1 = 15^o$ and $M_\infty = 0.94$, $\alpha_1 = 20^o$. Figure 14 shows oil flow simulation over payload shroud of SLV-7. The flow attachment can be noticed by the accumulation of oil and it compares well with the experimental results.

Wall Pressure fluctuations

Figure 15 shows variation of pressure coefficient along payload shroud of SLV-7. The surface pressure coefficient shows the effect of freestream Mach numbers.

Shock induced separation. All the essential features of transonic flow are well captured and a separation zone is observed in the cylinder region. The unsteady flow computation is continued till some anticipated periodicity in the flow variables is observed. The study of the flow field in the cylinder region, the shock locations, computed the surface pressure levels and the frequency content.

The figure depicts a close-up view of the velocity field in the hemisphere-cylinder body. It can be seen from the velocity vector plots that the flow separates at the junction of the hemisphere-cylinder

enclosing a recirculation region of low velocity. The comparison between present results with experimental data shows some disagreement on the cylindrical region of the heat shield at M_∞ = 1.2. This is attributed to pressure loss along the expansion fan, poor recovery of the pressure and separated flow on the boat tail region of the heat shield.

Figure 16 shows variation of pressure coefficient along payload shroud of SLV-7 at supersonic speeds. The pressure coefficient in the boat tail region shows formation of bucket that will influence reattachment point of the separated flow.

Payload fairing of SLV exhibits high levels of pressure fluctuations at transonic speeds attributed to shock-wave/turbulent boundary-layer interactions (SWTBLI) and associated with separated flow and formation of a vortex pair. One of the main attributed to transonic shock-wave/boundary-layer interactions featuring intermittently attached separated flows over the payload shroud region of a satellite launch vehicle.

It has been found that the nose-cone semi-angle is an important parameter that influences the development of unsteady flow over the payload region of a launch-vehicle model. We will discussed computation of acoustic load in the next section.

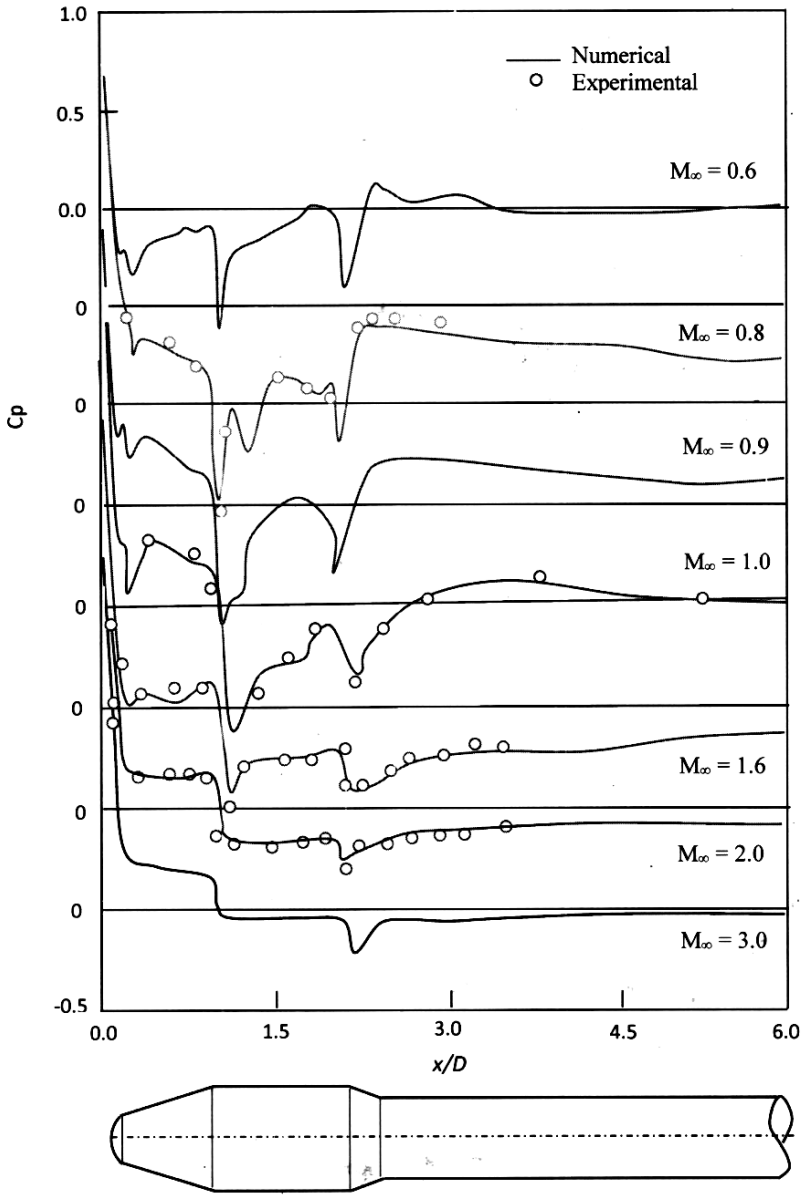

Fig 15: Variation of pressure coefficient along payload shroud of SLV-7

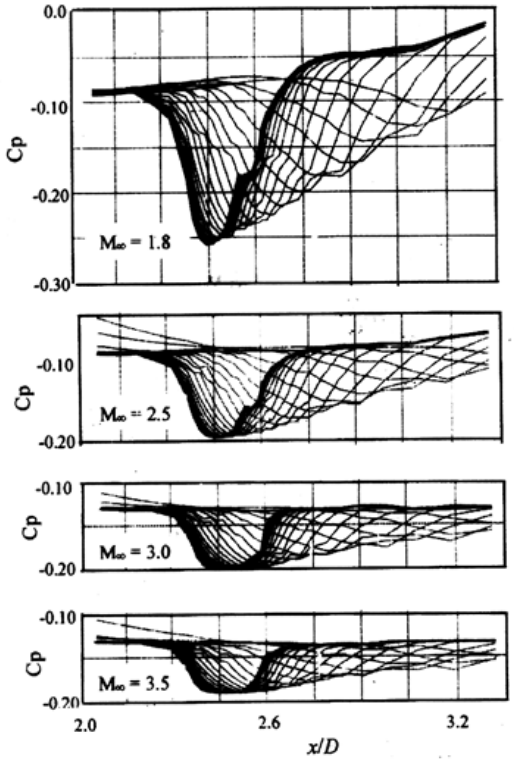

Fig 16: Variation of pressure coefficient along payload shroud of SLV-7 at supersonic speeds

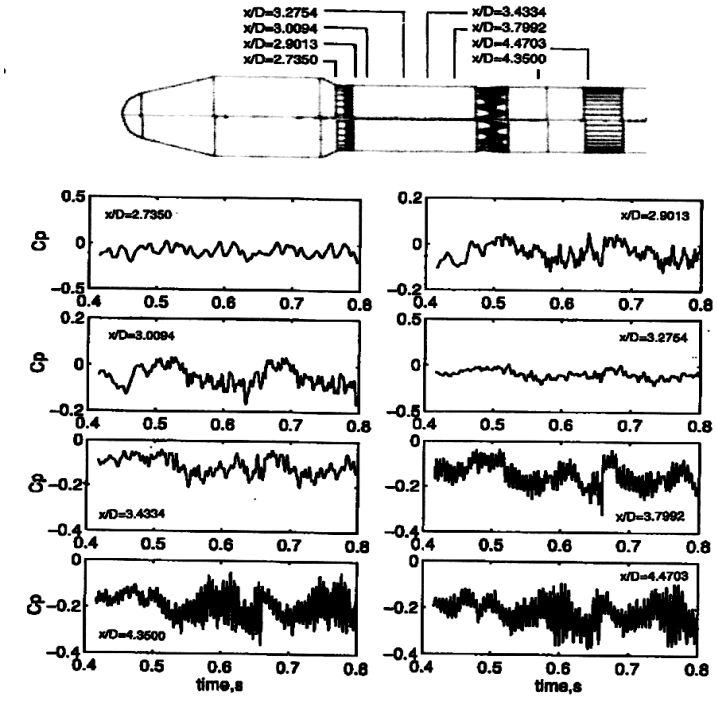

Fig 17: Variation of unsteady pressure coefficient at M_∞ = 0.90 payload shroud of SLV-7

Table 10: Sound pressure level (SPL) for payload shroud of SLV-7

M_∞	0.80	0.85	0.90	0.95	1.0	1.1
SPL dB	158.6	158.0	157.6	153.7	158.2	158.4

Sound pressure level analysis

The main focus of solving RANS equations is to analysis unsteady flow field [26] behaviour over SLV-7. Digital spectrum analysis associates with computed pressure coefficient is carried out using Fast Fourier Transform of MATLAB [27]. Figure 17 shows variation of unsteady pressure coefficient at M_∞ = 0.90 payload shroud of SLV-7. The characteristic time of the flow is $D/u_\infty = 2.68 \times 10^{-4}$ s

Before the analysis of the amplification factor and sound pressure levels was initiated, a statistical approach was used in order to ensure that the data are free from transitional phase, i.e., the pressure values are representative of the data, if the computation had continued for a long time. The calculated surface pressure data are analyzed for time mean and root mean square (rms) values. The value of m and Δt are 9800 and 7.10×10^{-7}s, respectively, where m is the number of steps at each sampling station, and Cp is ensemble average. The fluctuations of pressure coefficient are not amplified through the reattachment of turbulent boundary layer. To ensure further that the data are free from transitional phase, i.e., the pressure values are representative of the data, the computations are continued for a long time period.

The spectral analysis is carried out on the computed pressure-time data for all possible modes of fluctuations employing fast Fourier transform of MATLAB [27], which concerns the pressure history from time domain into frequency domain. The pressure values have been converted from Pascal to decibel (dB) of surface pressure levels. The surface pressure levels are computed in terms of the rms pressure reference 20 μPa. Table 10 depicts sound pressure level (SPL) for payload shroud of SLV-7. It will be useful for acoustic and buffet analysis of payload shroud of satellite launch vehicle.

CONCLUSIONS

The flowfields over the body are simulated numerically three-dimensional compressible Euler equations. The aerodynamic coefficients over various payload fairing of satellite launch vehicle are computed for structural design at Mach 1.2 and 1.8 corresponding at maximum aerodynamic drag and dynamic pressure, respectively. The computed data applicable to estimation of flow direction during the ascent phase of launch vehicle. The preliminary design of payload fairing can be applied using CFD approach to satisfy the structural requirement in conjunction with the NASA payload design criteria. It will reduce number of wind tunnel testing of the payload shroud.

A numerical result of axisymmetric turbulent viscous flow over a payload shroud is presented by using a multi-stage Runge-Kutta time-stepping scheme. Turbulence closure is achieved using algebraic turbulence model. The flow field visualization of the terminal shock and separated region adds in a systematic understanding of the unsteady flow characteristics under various freestream Mach numbers and various payload shroud geometry. The terminal shock moves downstream with increasing freestream Mach number. The location of the terminal shock is tabulated as a function of freestream Mach number. The separation zone in the boat tail region is found as a function of freestream Mach number and Reynolds number.

REFERENCES

1. Cole Jr, H. A., Erickson, A. L., & Rainey, A. G. (1970). Buffeting during atmospheric ascent. *NASA SP-8001, Nov*.
2. Muraca, R. J. (1966). *An empirical method for determining static distributed aerodynamic loads on axisymmetric multistage launch vehicles*. National Aeronautics and Space Administration.
3. Sooy, T. J., & Schmidt, R. Z. (2005). Aerodynamic predictions, comparisons, and validations using missile datcom (97) and aeroprediction 98 (ap98). *Journal of spacecraft and rockets*, *42*(2), 257-265.
4. Blevins, J. A., Campbell Jr, J. R., Bennett, D. W., Rausch, R. D., Gomez, R. J., & Kiris, C. C. (2014, January). An Overview of the Characterization of the Space Launch Vehicle Aerodynamic Environments. In *AIAA SciTech 2014 Conference* (No. M13-3142).
5. Hall, L., Eppard, W., Applebaum, M., & Blevins, J. A. (2011). Cartesian Euler code application for launch vehicle systems, 49th AIAA Aerospace Sciences Meeting including the new Horizon forum and Aerospace Exposition.
6. Pinier, J. T., Bennett, D. W., Blevins, J. A., Erickson, G. E., Faveregh, N. M., Houlden, H. P., & Tomek, W. G. (2014). Space launch system ascent static aerodynamic database development, 52nd AIAA Aerospace Sciences Meetings.
7. Bigarella, E. D. V., Azevedo, J. L. F., & Mello, O. A. F. (2004). Normal force calculations for rocket-like configurations. *Journal of the Brazilian Society of Mechanical Sciences and Engineering*, *26*(3), 290-296.
8. Brower, T. L. (2006). Titan launch vehicle: Ground test history. *Journal of spacecraft and rockets*, *43*(1), 147-160.
9. Pritchett, V. E., Maybe, M. N., Blevins, J. A., Crosby, W. A., & Purinton, D. C. (2014). Aerodynamic tests of the space launch system for database development, 52nd AIAA Aerospace Sciences Meetings.
10. Ozair, M., Jamshed, S., & Qureshi, M. N. (2017, November). Time-accurate CFD simulation of transonic flow over a hammerhead nose cone configuration. In *2017 Fifth International Conference on Aerospace Science & Engineering (ICASE)* (pp. 1-6). IEEE.

11. Liu, Y., Wang, G., Zhu, H., & Ye, Z. (2019). Numerical analysis of transonic buffet flow around a hammerhead payload fairing. *Aerospace Science and Technology*, *84*, 604-619.
12. Yanamashetti, G., Suryanarayana, G. K., & Mukherjee, R. (2017, March). Development of Flow over Blunt-Nosed Slender Bodies at Transonic Mach Numbers. In *Journal of Physics: Conference Series* (Vol. 822, No. 1, p. 012071). IOP Publishing.
13. Sunil, K., Johri, I., & Priyadarshi, P. (2022). Aerodynamic Shape Optimization of Payload Fairing Boat Tail for Various Diameter Ratios. *Journal of Spacecraft and Rockets*, 1-14.
14. Jiang, L., Yu, X., Wang, C., Dai, T., Dai, Z., & Tong, S. (2021). Analysis of Imaging Quality of New Laser Communication System on Missile in the Aerodynamic Environment. *Journal of Russian Laser Research*, *42*(2), 210-218.
15. Alter, S. J., Brauckmann, G. J., Kleb, W. L., Streett, C., & Glass, C. (2015). Time-Accurate Unsteady Pressure Loads Simulated for the Space Launch System at Wind Tunnel Conditions, 33rd AIAA Applied Aerodynamics Conference, AIAA Paper 2015-3149. https://doi.org/10.2514/6.2015-3149
16. Brauckmann, G. J., Streett, C., Kleb, W. L., Alter, S. J., Murphy, K. J., & Glass, C. (2015). Computational and Experimental Unsteady Pressures for Alternate SLS Booster Nose Shapes, 53rd AIAA Aerospace Sciences Meeting, AIAA Paper 2015-0559. https://doi.org/10.2514/6.2015-0559
17. Mehta, R. C. (2014). Unsteady Flowfield Characteristics over Blunt Bodies at High Speed," Computational and Numerical Simulations, edited by J. Awrejcewicz, IntechOpen, London, 83–117. https://doi.org/10.5772/57050
18. Sekula, M. K., Piatak, D. J., & Rausch, R. D. (2012). Analysis of Ares Crew Launch Vehicle Transonic Alternating Flow Phenomenon. *Journal of Spacecraft and Rockets*, *49*(5), 788-797.
19. Piatak, D. J., Sekula, M. K., & Rausch, R. D. (2012). Ares launch vehicle transonic buffet testing and analysis techniques. *Journal of Spacecraft and Rockets*, *49*(5), 798-807.
20. Dotson, K. W., & Engblom, W. A. (2004). Vortex-induced vibration of a heavy-lift launch vehicle during transonic flight. *Journal of fluids and structures*, *19*(5), 669-680.
21. Jiang, L., Yu, X., Wang, C., Dai, T., Dai, Z., & Tong, S. (2021). Analysis of Imaging Quality of New Laser Communication System on Missile in the Aerodynamic Environment. *Journal of Russian Laser Research*, *42*(2), 210-218.
22. Jameson, A., Schmidt, W., & Turkel, E. (1981, June). Numerical solution of the Euler equations by finite volume methods using Runge Kutta time stepping schemes. In *14th fluid and plasma dynamics conference* (p. 1259).
23. Mehta, R. C. (2017). Multi-block structured grid generation method for computational fluid dynamics. *Scholars J. Eng. Technol*, *5*(8), 387-393.
24. Kordulla, W., & Vinokur, M. (1983). Efficient computation of volume in flow predictions. *Aiaa Journal*, *21*(6), 917-918.
25. Baldwin, B., & Lomax, H. (1978, January). Thin-layer approximation and algebraic model for separated turbulentflows. In *16th aerospace sciences meeting* (p. 257).
26. Marple, Jr. S. L. (1987). Digital Spectrum Analysis with Applications, Prentice-Hall Inc., NJ.
27. MATLAB User's guide, pp. 2.47-2.51, The Math Works Inc, USA, 1992.